Available online at www.sciencedirect.com
ScienceDirect
Journal of Sound and Vibration 324 (2009) 587–607
JOURNAL OF SOUND AND VIBRATION
www.elsevier.com/locate/jsvi

Acoustic source property prediction based on near-field measurements in planar coordinate

Yong Thung Cho[a,*], J. Stuart Bolton[a], Michael J. Roan[b]

[a]*Ray W. Herrick Laboratories, School of Mechanical Engineering, Purdue University, 140 South Martin Jischke Drive, West Lafayette, IN 47907-2031, USA*
[b]*Vibration and Acoustics Laboratories, Department of Mechanical Engineering, Virginia Polytechnic Institute and State University, Blacksburg, VA 24061-0238, USA*

Received 4 April 2008; received in revised form 19 August 2008; accepted 23 February 2009
Handling Editor: R.J. Astley
Available online 26 March 2009

Abstract

Near-field acoustical holography (NAH) can be used to predict the acoustical properties of noise sources by starting from measurements of near-field pressures. In particular, the sound pressure, particle velocity, and intensity can all be estimated on a source plane. In the present work, an equation relating acoustical source properties and the pressure radiated from a source is derived from the Kirchoff–Helmholtz integral equation and is here referred to as the inverse Rayleigh method. The inverse Rayleigh method reduces to the Rayleigh integral when the source is located on an infinite rigid baffle. However, the same equation can also be used to predict the acoustic properties of a source in a more general environment: i.e., without assuming the presence of an infinite rigid baffle. In this article, the inverse Rayleigh method is described and then its relative accuracy is compared with other procedures that can be used to predict source particle velocity from near-field pressure measurements on a planar hologram. By comparing the accuracy of the present NAH method with other procedures in the case of a large hologram, it was found that the inverse Rayleigh method is accurate and computationally efficient for predicting the source particle velocity from near-field pressure measurements both with and without a rigid baffle.
© 2009 Elsevier Ltd. All rights reserved.

1. Introduction

Near-field acoustical holography (NAH) techniques can be used to estimate sound pressure, particle velocity, and intensity on a source surface (and surfaces that lie between the source and the measurement surface) based on measurements of the near-field pressure [1–3]. However, if the reconstruction of those quantities is to be accurate, it is required that the measurement aperture (i.e., the hologram surface) extend well beyond the source region to avoid spatial Fourier transform-related truncation effects [1–3]. If it is not possible to extend the measurement surface into the region where the sound pressure drops to sufficiently low

*Corresponding author. Tel.: +1 585 275 5069; fax: +1 585 273 4919.
E-mail address: cho.yong@gmail.com (Y.T. Cho).

0022-460X/$ - see front matter © 2009 Elsevier Ltd. All rights reserved.
doi:10.1016/j.jsv.2009.02.033

levels, owing to physical obstructions, for example, it is not possible to perform accurate projections by using conventional NAH.

Statistically optimized near-field acoustical holography (SONAH), originally derived in a planar formulation by Steiner and Hald [4] and later following a simpler approach by Hald [5], was developed to accommodate situations in which the measurement aperture size was limited either by physical necessity or as a way of limiting measurement effort. In the SONAH procedure, surface-to-surface projection of the sound field is performed by using a transfer matrix defined in such a way that all propagating waves and a weighted set of evanescent waves are projected with optimal average accuracy (i.e., no spatial Fourier transforms are performed) [4–6]. In this way, the requirement that the measurement surface extend well beyond the source region can be eliminated without necessarily compromising the accuracy of the procedure.

An alternative approach to the spatial truncation problem is offered by an iterative procedure referred to as patch holography, which was first suggested by Saijyou and Yoshikawa [7,8], and further developed by other investigators [9–11]. The effect of the patch procedure is to create a smooth transition of the sound field from the measured "patch" region to an extrapolated region. Then, the extrapolated measurement pressure is combined with conventional NAH procedures to project the sound field closer to or farther away from the source. Non-iterative procedures can also be applied to extrapolate the measurement pressure [12–19]. However, patch holography procedures were not applied in present work since it was possible to make measurement on a sufficiently large hologram to avoid truncation effects in simulation.

In the past, methods based on the Rayleigh integral have frequently been used to predict far-field pressure when the particle velocity of sources located on a rigid baffle was known [3,18,20]. However, that approach can also been used in an inverse sense to predict source particle velocities based on near-field pressure measurements if appropriate regularization techniques are used [18,21]. It is the latter approach that is pursued here.

The present work is also related to the method of wave superposition originally suggested by Koopman et al. [22] in which a relationship between a "fictional" source strength and the radiated pressure field was derived from the Kirchoff–Helmholtz integral (KHI) [23,24]. In that work, it was assumed that the fictional source strength was dependent only on source location when estimating the pressure field from source particle velocity measurements or *vice versa*. The method of wave superposition is similar to the Rayleigh integral approach except for the fact that the field pressure is related to the source strength on a virtual source surface in the former method instead of an actual particle velocity on an infinite source plane in the latter method. The method of wave superposition (also referred to as the "equivalent source method") has been implemented to predict the acoustic field from pressure measurements for several types of sources and measurement configurations [12,13,25–27].

The present work shares one goal with previous work [22], that is, to derive an equation relating acoustical source variables to the radiated pressure by starting from the KHI. Here, the KHI equation is solved for planar sources with measurements made in a geometry conformal with the source geometry. It has been found that a property, referred to as "source strength" in Ref. [22] and "fictitious source particle velocity" in this work, is dependent on measurement position, projection distance, and source location. It is shown that by introducing a virtual source plane, the dependence of the fictitious source particle velocity on measurement location and projection distance is reduced. The fictitious source particle velocity is estimated by using a regularized least square solution that is optimal for the measurement pressure and location and geometry of hologram. The fictitious source particle velocity reduces to the source particle velocity as in the Rayleigh integral when the source is located on an infinite planar rigid baffle [23]. The present work is also similar in some respects to previous work by Nelson and Yoon [28], who sought to identify the strength of fictional sources from the radiated pressure by inverting the transfer matrix between the sources and the radiated pressure. Regularization procedures for more accurate estimation of source properties were extensively investigated by Nelson and Yoon [28]: in contrast, the relationship between source properties and radiated pressure is investigated in detail in the present work.

In this article, the relative accuracy of the inverse Rayleigh and other procedures for estimating source particle velocities from near-field pressure measurements on a planar hologram are quantified by comparing known particle velocities and predictions from near-field pressure measurements in both numerical simulations and experiments. In the experimental work, the source particle velocity of a baffled aluminum plate was measured

directly with accelerometers and compared with particle velocities estimated from near-field measurements. Comparisons between direct source particle velocity measurements and predictions were made in terms of mean square error. These results are shown in Sections 3–5. First, though, the theoretical background for the source velocity estimation procedures is given in the next section.

2. Particle velocity prediction methods based on near-field measurements

In this section, an equation for source particle velocity prediction based on near-field measurements is derived from the KHI. As noted above, the relationship between source particle velocity and the measurement pressure reduces to the Rayleigh integral when the source is located on infinite rigid planar baffle. The source particle velocity can also be estimated by using existing procedures such as NAH and SONAH. Even though SONAH is a more recently derived procedure than conventional NAH, both NAH and SONAH use the same propagator in planar implementations, so the accuracy of both procedures should be very similar if the effect of spatial truncation of the measurement pressure is negligible. In previous work, the NAH [1–3] and SONAH [4,5] procedures were derived in detail, and the derivation of SONAH in planar coordinates was given in Ref. [29], so those procedures are not presented in detail in this work. Note that the conventional NAH calculations presented here were performed as they would have been in an experimental situation: i.e., a spatial, Tukey window was applied to the data to smooth the transition at the edges of the aperture and the spatial data was then zero-padded. In addition, conventional wave number filtering procedures were applied. In the latter procedure, a low pass spatial filter is specified by its cutoff wave number, k_c [1–3]. All filtering parameters were adjusted until the lowest mean square projection error of each procedure was achieved. This was done to ensure that comparisons were made based on the best performance of each holography procedure.

2.1. Derivation of relation between source property and measurement pressure

The Rayleigh integral, derived from the KHI theorem, can be used to predict far-field pressure or source particle velocity from near-field pressure measurements for sources located on an infinite rigid baffle. The Rayleigh integral is not valid and less accurate for predicting sound field properties if the source is not located on infinite rigid baffle.

The sound pressure, p, at arbitrary locations can be predicted using the KHI theorem if the velocity and pressure of the source are known [23]: i.e.,

$$G(\nabla^2 + k^2)p - p(\nabla^2 + k^2)G = \nabla \cdot (G\nabla p - p\nabla G), \tag{1}$$

where G is the Green's function for the Helmholtz equation, k is the wave number, and ∇ is the gradient vector operator. The pressure satisfying the Helmholtz equation exterior to the source is

$$p(\mathbf{r}) = -\frac{1}{4\pi}\int\int (G\nabla p - p\nabla G)\cdot \mathbf{n}_s \,\mathrm{d}S, \tag{2}$$

where $\mathbf{n}_s$ is a unit vector normal to the source surface. Alternatively, if the source is located on the z-plane, Eq. (2) can be expressed as

$$p(\mathbf{r}) = \frac{1}{4\pi}\int\int [p(\mathbf{r}_s)\nabla_s G(\mathbf{r}_s|\mathbf{r}) - G(\mathbf{r}_s|\mathbf{r})\nabla_s p(\mathbf{r}_s)]\cdot \mathbf{e}_z \,\mathrm{d}S, \tag{3}$$

where $\mathbf{e}_z$ is a unit vector in the z-direction and ∇_s denotes the gradient in the direction normal to the source surface. The definition of the coordinate system for the derivation of the Rayleigh integral and the relationship between the geometry of the source and measurement planes is shown in Fig. 1. When using an $\mathrm{e}^{-\mathrm{i}\omega t}$ sign convention, and if point source and free field conditions are assumed, the Green's function is [24]

$$G(\mathbf{r}_s|\mathbf{r}) = \mathrm{e}^{\mathrm{i}kR}/R, \tag{4}$$

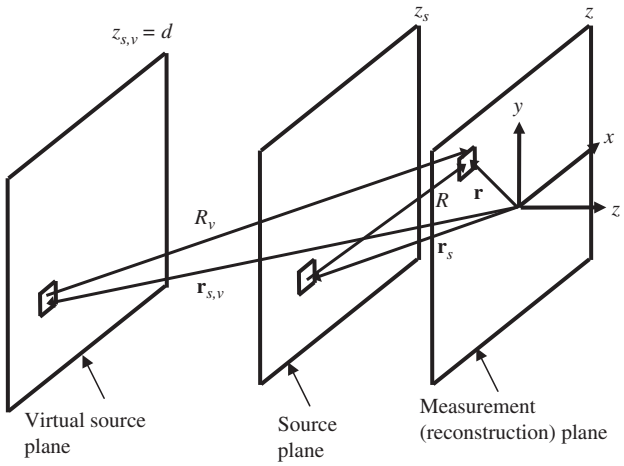

Fig. 1. Definition of source and near-field measurement geometry with a virtual source plane.

with the result that

$$\nabla_s G(\mathbf{r}_s|\mathbf{r}) = \frac{(\mathbf{r}_s - \mathbf{r})}{R^3}(-1 + \mathrm{i}kR)\,\mathrm{e}^{\mathrm{i}kR}, \tag{5}$$

$$\nabla_s G(\mathbf{r}_s|\mathbf{r}) \cdot \mathbf{e}_z = \frac{(z_s - z)}{R^3}(-1 + \mathrm{i}kR)\,\mathrm{e}^{\mathrm{i}kR}. \tag{6}$$

By using Euler's equation, the pressure and normal particle velocity can be related: i.e.,

$$\nabla_s p(\mathbf{r}_s) \cdot \mathbf{e}_z = \mathrm{i}\rho\omega u_z(\mathbf{r}_s). \tag{7}$$

By combining Eqs. (3)–(7), the solution of the KHI theorem reduces to

$$p(\mathbf{r}) = -\frac{\mathrm{i}\rho\omega}{4\pi}\int\int \frac{e^{\mathrm{i}kR}}{R}\left[\frac{p(\mathbf{r}_s)}{\rho c}\left(\frac{1}{\mathrm{i}kR} - 1\right)\frac{z_s - z}{R} + u_z(\mathbf{r}_s)\right]\mathrm{d}S. \tag{8}$$

Here, a new quantity called the fictitious velocity, $\mathbf{u}_{\mathrm{fic}}(\mathbf{r}_s,\mathbf{r})$, is introduced. It is defined as

$$\mathbf{u}_{\mathrm{fic},z}(\mathbf{r}_s, \mathbf{r}) = \frac{p(\mathbf{r}_s)}{\rho c}\left(\frac{1}{\mathrm{i}kR} - 1\right)\frac{z_s - z}{R} + u_z(\mathbf{r}_s). \tag{9}$$

By using the fictitious velocity, the pressure estimated using the KHI becomes

$$p(\mathbf{r}) = -\frac{\mathrm{i}\rho\omega}{4\pi}\int\int \frac{\mathrm{e}^{\mathrm{i}kR}}{R}\mathbf{u}_{\mathrm{fic},z}(\mathbf{r}_s, \mathbf{r})\,\mathrm{d}S. \tag{10}$$

If a virtual source plane is introduced as shown in Fig. 1, and a fictitious normal source particle velocity is estimated on the virtual instead of the actual source plane, then Eqs. (9) and (10) become

$$\mathbf{u}_{\mathrm{fic},z}(\mathbf{r}_{s,v}, \mathbf{r}) = \frac{p(\mathbf{r}_{s,v})}{\rho c}\left(\frac{1}{\mathrm{i}kR_v} - 1\right)\frac{z_{s,v} - z}{R_v} + u_z(\mathbf{r}_{s,v}), \tag{11}$$

$$p(\mathbf{r}) = -\frac{\mathrm{i}\rho\omega}{4\pi}\int\int \frac{\mathrm{e}^{\mathrm{i}kRv}}{R_v}\mathbf{u}_{\mathrm{fic},z}(\mathbf{r}_{s,v}, \mathbf{r})\,\mathrm{d}S. \tag{12}$$

It is important to note that the introduction of a virtual source plane farther away from the actual source plane reduces the magnitude of the near field components in the fictitious normal source particle velocity and makes it possible to estimate the pressure or particle velocity on the actual source plane by combining back and forward projection of measurement pressure.

When comparing Eqs. (9)–(12) with the method of wave superposition, it can be seen that the fictitious normal source particle velocity is dependent on the measurement location rather than being dependent only on the source location as originally suggested by Koopman et al. [22]. The partial derivative of the fictitious normal source particle velocity with respect to measurement surface location, z, is presented in Appendix A. It is shown there that the amplitude of the derivative of the fictitious normal source particle velocity is reduced when the virtual source surface is located further away from the actual source. This is also true when the measurement or reconstruction surface is located further away from the actual source. So, by introducing a virtual source plane, the dependence of the fictitious source particle velocity on measurement location and projection distance is reduced. The fictitious source particle velocity is estimated by using a regularized least square solution that is optimal for the measurement pressure and location and geometry of the hologram.

Eq. (10) differs from the Rayleigh integral in that a fictitious source particle velocity is used, and the fictitious source particle velocity is a function of both source and measurement location. In contrast, the Rayleigh integral is

$$p(\mathbf{r}) = -\frac{\mathrm{i}\rho\omega}{2\pi}\int\int\frac{\mathrm{e}^{\mathrm{i}kR}}{R}\mathbf{u}_z(\mathbf{r}_s)\,\mathrm{d}S, \tag{13}$$

and the source particle velocity is a function only of source location and is independent of measurement location. Eq. (8) reduces to the Rayleigh integral for sources located on an infinite rigid baffle. A detailed description of the discretization and the estimation of the regularized inverses of both Eqs. (10) and (13) are presented next.

2.2. Discretization of the relation between source property and measurement pressure

Eq. (10) can be expressed in explicit, discretized form as

$$\begin{aligned}
p_1 &= -\frac{\mathrm{i}\omega\rho_0\Delta x_s\Delta y_s}{4\pi}\left[\, w_1\frac{\mathrm{e}^{\mathrm{i}kR_{v11}}}{R_{v11}} \quad w_2\frac{\mathrm{e}^{\mathrm{i}kR_{v12}}}{R_{v12}} \quad \cdots \quad w_N\frac{\mathrm{e}^{\mathrm{i}kR_{v1N}}}{R_{v1N}}\,\right] \\
&\qquad \times\left[u_{\mathrm{fic},z,sv11}\ \ u_{\mathrm{fic},z,sv12}\ \ \cdots\ \ u_{\mathrm{fic},z,sv1N}\right]^{\mathrm{T}}, \\
p_2 &= -\frac{\mathrm{i}\omega\rho_0\Delta x_s\Delta y_s}{4\pi}\left[\, w_1\frac{\mathrm{e}^{\mathrm{i}kR_{v21}}}{R_{v21}} \quad w_2\frac{\mathrm{e}^{\mathrm{i}kR_{v22}}}{R_{v22}} \quad \cdots \quad w_N\frac{\mathrm{e}^{\mathrm{i}kR_{v2N}}}{R_{v2N}}\,\right] \\
&\qquad \times\left[u_{\mathrm{fic},z,sv21}\ \ u_{\mathrm{fic},z,sv22}\ \ \cdots\ \ u_{\mathrm{fic},z,sv2N}\right]^{\mathrm{T}}, \\
&\qquad\qquad \vdots \\
p_M &= -\frac{\mathrm{i}\omega\rho_0\Delta x_s\Delta y_s}{4\pi}\left[\, w_1\frac{\mathrm{e}^{\mathrm{i}kR_{vM1}}}{R_{vM1}} \quad w_2\frac{\mathrm{e}^{\mathrm{i}kR_{vM2}}}{R_{vM2}} \quad \cdots \quad w_N\frac{\mathrm{e}^{\mathrm{i}kR_{vMN}}}{R_{vMN}}\,\right] \\
&\qquad \times\left[u_{\mathrm{fic},z,svM1}\ \ u_{\mathrm{fic},z,svM2}\ \ \cdots\ \ u_{\mathrm{fic},z,svMN}\right]^{\mathrm{T}},
\end{aligned} \tag{14}$$

where Δx_s and Δy_s are the measurement spacings on the source plane in the x- and y-directions, respectively, w_j is an appropriate weighting for estimating the integrals depending on the order of integration [30], $R_{i,j}$ is the distance from a point on the source $(x_{sj},y_{sj},0)$ to a position on the hologram (x_i,y_i,z), which is $R_{i,j} = [(x_i-x_{sj})^2+(y_i-y_{sj})^2+z^2]^{1/2}$, N is the total number of reconstruction points on the source surface, and M is the total number of measurement points on the hologram or reconstruction surface. Similarly, $R_{vi,j}$ is the distance from a point on the virtual source plane (x_{svj},y_{svj},z_{sv}) to a position on the hologram (x_i,y_i,z), and it is given by $R_{vi,j} = [(x_i-x_{svj})^2+(y_i-y_{svj})^2+(z-z_{sv})^2]^{1/2}$.

By introducing the optimal fictitious source particle velocity for the measurement pressure, Eq. (14) becomes

$$\begin{bmatrix} p_1+\varepsilon(p_1) \\ p_2+\varepsilon(p_2) \\ \vdots \\ p_M+\varepsilon(p_M) \end{bmatrix} = -\frac{\mathrm{i}\omega\rho_0\Delta x_s\Delta y_s}{4\pi}\begin{bmatrix} w_1\frac{\mathrm{e}^{\mathrm{i}kR_{v11}}}{R_{v11}} & w_2\frac{\mathrm{e}^{\mathrm{i}kR_{v12}}}{R_{v12}} & \cdots & w_N\frac{\mathrm{e}^{\mathrm{i}kR_{v1N}}}{R_{v1N}} \\ w_1\frac{\mathrm{e}^{\mathrm{i}kR_{v21}}}{R_{v21}} & w_2\frac{\mathrm{e}^{\mathrm{i}kR_{v22}}}{R_{v22}} & \vdots & w_N\frac{\mathrm{e}^{\mathrm{i}kR_{v2N}}}{R_{v2N}} \\ \vdots & \vdots & \vdots & \vdots \\ w_1\frac{\mathrm{e}^{\mathrm{i}kR_{vM1}}}{R_{vM1}} & w_2\frac{\mathrm{e}^{\mathrm{i}kR_{vM2}}}{R_{vM2}} & \cdots & w_N\frac{\mathrm{e}^{\mathrm{i}kR_{vMN}}}{R_{vMN}} \end{bmatrix} \times \begin{bmatrix} u_{\mathrm{opt,fic},z,sv1} \\ u_{\mathrm{opt,fic},z,sv2} \\ \vdots \\ u_{\mathrm{opt,fic},z,svN} \end{bmatrix}, \tag{15}$$

where $\varepsilon(p_i)$ is the error in the reconstructed pressure on the measurement surface due to the substitution of a fictitious source particle velocity dependent on measurement location for the fictitious source particle velocity dependent only on source location. For the purpose of finding the optimal fictitious source particle velocity, the error in the reconstructed pressure on the measurement surface is approximated as zero, and Eq. (15) can be approximated as

$$\begin{bmatrix} p_1 \\ p_2 \\ \vdots \\ p_M \end{bmatrix} = -\frac{\mathrm{i}\omega\rho_0\Delta x_s\Delta y_s}{4\pi}\begin{bmatrix} w_1\frac{\mathrm{e}^{\mathrm{i}kR_{v11}}}{R_{v11}} & w_2\frac{\mathrm{e}^{\mathrm{i}kR_{v12}}}{R_{v12}} & \cdots & w_N\frac{\mathrm{e}^{\mathrm{i}kR_{v1N}}}{R_{v1N}} \\ w_1\frac{\mathrm{e}^{\mathrm{i}kR_{v21}}}{R_{v21}} & w_2\frac{\mathrm{e}^{\mathrm{i}kR_{v22}}}{R_{v22}} & \vdots & w_N\frac{\mathrm{e}^{\mathrm{i}kR_{v2N}}}{R_{v2N}} \\ \vdots & \vdots & \vdots & \vdots \\ w_1\frac{\mathrm{e}^{\mathrm{i}kR_{vM1}}}{R_{vM1}} & w_2\frac{\mathrm{e}^{\mathrm{i}kR_{vM2}}}{R_{vM2}} & \cdots & w_N\frac{\mathrm{e}^{\mathrm{i}kR_{vMN}}}{R_{vMN}} \end{bmatrix} \times \begin{bmatrix} u_{\mathrm{opt,fic},z,sv1} \\ u_{\mathrm{opt,fic},z,sv2} \\ \vdots \\ u_{\mathrm{opt,fic},z,svN} \end{bmatrix}, \tag{16}$$

i.e., the fictitious source particle velocity on the virtual source plane that is optimal for the measurement pressure is used in Eq. (16) instead of that shown in Eqs. (9) and (14), which is dependent on measurement and reconstruction location. The subscript of the fictitious source particle velocity on the virtual source plane in Eqs. (15) and (16) is changed to indicate that it is optimal for the reconstruction of measurement pressure on the measurement surface. From Eq. (16), the optimal fictitious source particle velocity on the virtual source plane can be estimated from pressure measurements by evaluating the regularized least square inverse of the transfer matrix in Eq. (16).

The use of an appropriate virtual source plane at location $z_v = d$ allows an estimation based on Eq. (16) to be more accurate; since $R_v > R$, the near-field term in Eq. (11) is smaller than that in Eq. (9): i.e., the variation of the fictitious source particle velocity due to distance R on the virtual source plane is smaller than that on the actual source plane. This approximation becomes more accurate when $KR_v \gg 1$ and $R_v \gg \Delta(z - z_{s,v})$. Under those conditions, the dependence of Eq. (11) on the distance R is reduced. However, the use of a larger R_v does not necessarily imply a more accurate estimation of Eq. (11) or (14). For example, cases in which the virtual source location is farther away from the actual source location may have decreased projection accuracy compared to cases where the virtual source location is closer to the actual source location. Therefore, an

optimal virtual source plane location, $z_v = d$, exists for a specific source and measurement configuration. This location depends on the wave number content and signal-to-noise ratio of the measurement pressure, geometry of the measurement surface, etc.

Once the optimal, regularized least square fictitious source particle velocity is estimated on the virtual source plane, the pressure on any surface beyond the actual source surface can be estimated by applying the appropriate transfer matrix. The Rayleigh integral shown in Eq. (13) can be expressed in explicit, discretized form as

$$\begin{bmatrix} p_1 \\ p_2 \\ \vdots \\ p_M \end{bmatrix} = -\frac{\mathrm{i}\omega\rho_0\Delta x_s\Delta y_s}{2\pi} \begin{bmatrix} w_1\frac{\mathrm{e}^{\mathrm{i}kR_{11}}}{R_{11}} & w_2\frac{\mathrm{e}^{\mathrm{i}kR_{12}}}{R_{12}} & \cdots & w_N\frac{\mathrm{e}^{\mathrm{i}kR_{1N}}}{R_{1N}} \\ w_1\frac{\mathrm{e}^{\mathrm{i}kR_{21}}}{R_{21}} & w_2\frac{\mathrm{e}^{\mathrm{i}kR_{22}}}{R_{22}} & \vdots & w_N\frac{\mathrm{e}^{\mathrm{i}kR_{2N}}}{R_{2N}} \\ \vdots & \vdots & \vdots & \vdots \\ w_1\frac{\mathrm{e}^{\mathrm{i}kR_{M1}}}{R_{M1}} & w_2\frac{\mathrm{e}^{\mathrm{i}kR_{M2}}}{R_{M2}} & \cdots & w_N\frac{\mathrm{e}^{\mathrm{i}kR_{MN}}}{R_{MN}} \end{bmatrix} \times \begin{bmatrix} u_{z,s1} \\ u_{z,s2} \\ \vdots \\ u_{z,sN} \end{bmatrix}. \tag{17}$$

Finally, Eqs. (16) and (17) can be expressed in matrix form as

$$\mathbf{p} = \mathbf{C}_v\mathbf{u}_{\mathrm{opt,fic},z,sv}, \tag{18}$$

and,

$$\mathbf{p} = \mathbf{C}\mathbf{u}_{z,s}, \tag{19}$$

respectively, where $\mathbf{p}$ is a column vector of the measured or reconstructed pressures, $u_{z,s}$ is a column vector of the particle velocities on the source plane, and $\mathbf{C}$ is a transfer matrix relating the particle velocity on the source plane to the measured or reconstructed pressures. The quantity $\mathbf{u}_{\mathrm{opt,fic},z,sv}$ is a column vector consisting of the least square fictitious particle velocities on the virtual source plane, and $\mathbf{C}_v$ is a transfer matrix relating the fictitious particle velocities on the virtual source plane to the measured or reconstructed pressures.

The estimate of the particle velocity of a source on an infinite rigid baffle can be found by inverting the transfer matrix and multiplying it by the measurement pressure vector on the hologram: i.e.,

$$\mathbf{u}_{z,s} = \mathbf{C}^{-1}\mathbf{p}. \tag{20}$$

The estimate of the particle velocity may be corrupted by high wave number component noise that is amplified during backward projection. Here a least square regularization procedure is introduced that can reduce corruption during the inversion procedure. That regularization is implemented as

$$\mathbf{u}_{\mathrm{opt,fic},z,sv} \approx (\mathbf{C}_v^{\mathrm{H}}\mathbf{C}_v + \sigma^2\mathbf{I})^{-1}\mathbf{C}_v^{\mathrm{H}}\mathbf{p}, \tag{21}$$

where ^{H} denotes the Hermitian or conjugate transpose, $\mathbf{I}$ is the identity matrix, and the regularization parameter, σ, is, chosen to be [4,5]

$$\sigma^2 = [\mathbf{C}_v^{\mathrm{H}}\mathbf{C}_v]_{ii}10^{-\mathrm{SNR}/10}. \tag{22}$$

Both the inverse Rayleigh method and SONAH procedures require the choice of two regularization or filtering parameters: the position of the virtual source plane, d, and the signal-to-noise ratio, σ, that is comparable in effect to the cutoff wave number, k_c, that is used in conventional NAH. Eq. (21) represents the regularized least squares solution for the fictitious particle velocity on the virtual source plane.

To obtain accurate particle velocities from near-field pressure measurements, $\mathbf{u}_{\mathrm{opt,fic},z,sv}$ should be estimated on a virtual source plane and then forward projected to reconstruct the pressure on the actual source plane or

on any plane located away from the source using Eq. (18). The particle velocity on the actual source surface or any other plane can then be estimated by using Euler's equation: i.e.,

$$u_z(\mathbf{r}) = \frac{1}{\mathrm{i}\rho_0\omega}\frac{\partial p(\mathbf{r})}{\partial z}. \tag{23}$$

If the number of pressure and particle velocity measurements, M and N, in Eq. (14) are equal, then the number of elements in the transfer matrix is N^2. The transfer matrix has a large number of elements that are repeated, and the repetition of the elements in the transfer matrix is in the same form as in the SONAH matrix [6]. If the shape of the hologram is square, and the measurement spacings, Δx_s and Δy_s, are equal, only $\sqrt{N}(\sqrt{N}+1)/2$ elements are unique. By avoiding repeated calculations in the planar geometry, the number of calculations can be reduced by a factor of $2N$.

The particle velocity prediction procedure based on near-field pressure measurements that was presented in this section is referred to as the "inverse Rayleigh method" in this paper. It should be noted that the particle velocity estimated by using that procedure is different from that estimated using the inverse of the discretized Rayleigh integral in general. They are the same only for sources located on an infinite rigid planar baffle and when the pressure measurements are noise-free.

3. Baffled plate measurements

In Section 2, the procedure for prediction of particle velocity based on near-field measurements on a planar hologram was discussed. In this section, direct particle velocity measurements on the surface of a baffled aluminum plate are compared to particle velocities predicted by using NAH, SONAH and the inverse Rayleigh techniques operating on near-field pressure measurements.

3.1. Baffled plate measurement description

The source particle velocity and near-field pressure measurements were made on a point-driven, aluminum plate, 35 cm × 47 cm, mounted in a rigid baffle. Resonance frequencies were found by a tap test using a PCB impact hammer prior to source surface velocity measurements with the plate attached to the baffle. The shaker was driven by sinusoidal signals at 163 and 580 Hz, which corresponded to the (1,1) and (1,3) modes of the baffled plate, respectively. The baffled plate near-field measurement geometry is given in Fig. 2. Photographs of the plate and baffle used for the measurements are provided in Fig. 3. The near-field pressure measurement plane, i.e., the hologram, was 1.6 cm above the plate or source plane. It consisted of 25 × 27 measurements with a 2 cm microphone spacing both in the x- and y-directions. The measurement surface was a 50 cm × 54 cm rectangle for the near-field pressure measurements, and a 34 cm × 46 cm rectangle for the direct particle velocity measurements (consisting of 17 × 23 measurements with a 2 cm accelerometer spacing). The velocity

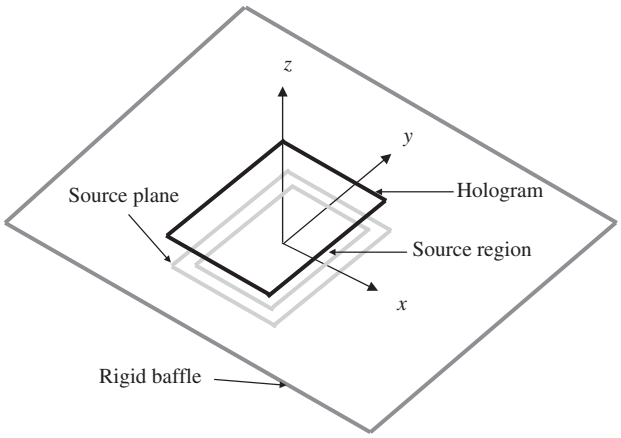

Fig. 2. Baffled plate near-field measurement geometry definition.

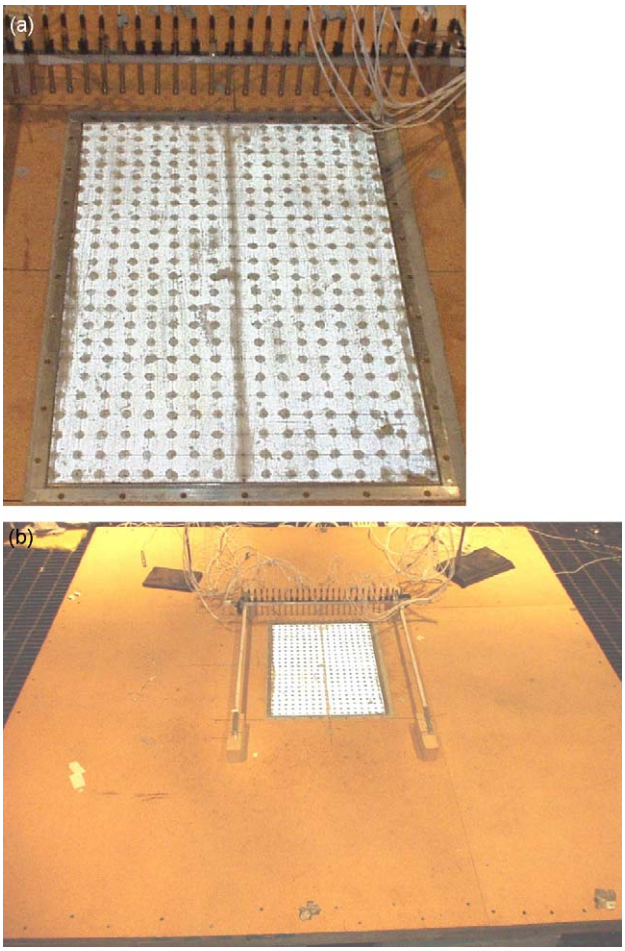

Fig. 3. Baffled plate source: (a) aluminum plate of 35 cm × 47 cm and (b) aluminum plate at the center of 1.8 m × 1.8 m square rigid baffle.

was measured over the entire source area of the baffled aluminum plate. The center of both the hologram and the source lay on the z-axis. The rigid baffle was 1.8 m × 1.8 square. The coordinate system origin was at the center of both the plate and baffle.

Twenty-five TMS T130C21 $\frac{1}{4}$-in microphones were used to make the near-field sound pressure measurements. Two PCB 353B17 accelerometers were attached to the plate to measure the velocity of the plate. The accelerometers were calibrated with a Brüel & Kjær accelerometer calibrator Type 4291 at 79.6 Hz, $1g$ peak acceleration.

A sinusoidal signal was computer generated and played through a JBL power amplifier Model 6230. A Wavetek Dual Hi/Lo filter Model 852 was used for low pass filtering of the sinusoidal signal with a cutoff frequency of 1000 Hz. The reference signal was taken directly from the output of the amplifier after it was low pass filtered. A Brüel & Kjær Mini Shaker Type 4810 was used to drive the center of the aluminum plate.

First, a $\frac{1}{4}$-in microphone was calibrated for level by using a G.R.A.S. Pistonphone Type 42AA, calibrating its amplitude at 250 Hz, 114 dB. Then, the other 24 scanning $\frac{1}{4}$-in microphones were calibrated both in amplitude and phase by using the Brüel & Kjær Z1 0055 Sound Intensity Calibrator over the entire frequency range of interest relative to the $\frac{1}{4}$-in microphone previously calibrated for level by using a G.R.A.S. Pistonphone.

Simultaneous near-field sound pressure measurements were made at 25 equally-spaced locations 1.6 cm above the baffled plate. These measurements covered the complete width of the hologram. The frequency range used for the sound pressure measurements was 0–2048 Hz. Twenty-seven sets of measurements were

made beginning at $y = -26$ cm and progressing to $y = 26$ cm in 2 cm increments. A Hanning window was applied to each time data record. The low pass filtered signals were fast Fourier transformed and were averaged 10 times to estimate the required transfer function between the output of the JBL amplifier and the microphone signals.

3.2. Near-field measurement results

The near-field sound pressure measurements above the baffled plate are shown in Fig. 4. The magnitudes of the frequency response functions (the H_1 transfer functions between the response of the microphones and the output of the JBL amplifier) representing the measured pressure amplitudes for the (1,1) and (1,3) modes of the plate are both shown in Fig. 4. Note that all of the measurement and prediction result figures in the present work were generated using Phong interpolation [31]. Although the measurements and predictions were made on a finite 2 cm spacing, the quantities themselves are continuous, and therefore were plotted using interpolation.

The velocity on the baffled plate source was measured with an accelerometer at the same two frequencies: 163 and 580 Hz. The magnitudes of the directly measured and back-projected source particle velocities based on the near-field pressure measurements 1.6 cm above the plate using the inverse Rayleigh, SONAH, and conventional NAH procedures are shown in Figs. 5 and 6.

The root mean square percentage error, which is referred to as mean square percentage error in the present work, is defined to compare the directly measured or true and predicted quantity as

$$\mathrm{MSE} = \sqrt{\frac{\sum_i |p_{t,i} - p_{s,i}|^2}{\sum_j |p_{t,j}|^2}} (\times 100), \tag{24}$$

where p_t is the directly "measured or true" quantity, and p_s is the estimated quantity from the near-field measurement. The mean square error between the directly measured and back-projected velocities for the three procedures is given in Table 1. The filtering parameter d in Table 1 is the position of the virtual source plane relative to the actual source plane along the z-axis.

The SONAH procedure gives back-projected source velocities in general agreement with the measured source velocities, and the magnitude of the back-projected velocity obtained by using SONAH is very small beyond the source region, as would be expected. The back-projected source velocity obtained by using conventional NAH differed considerably from the directly measured velocity, especially around the edge of

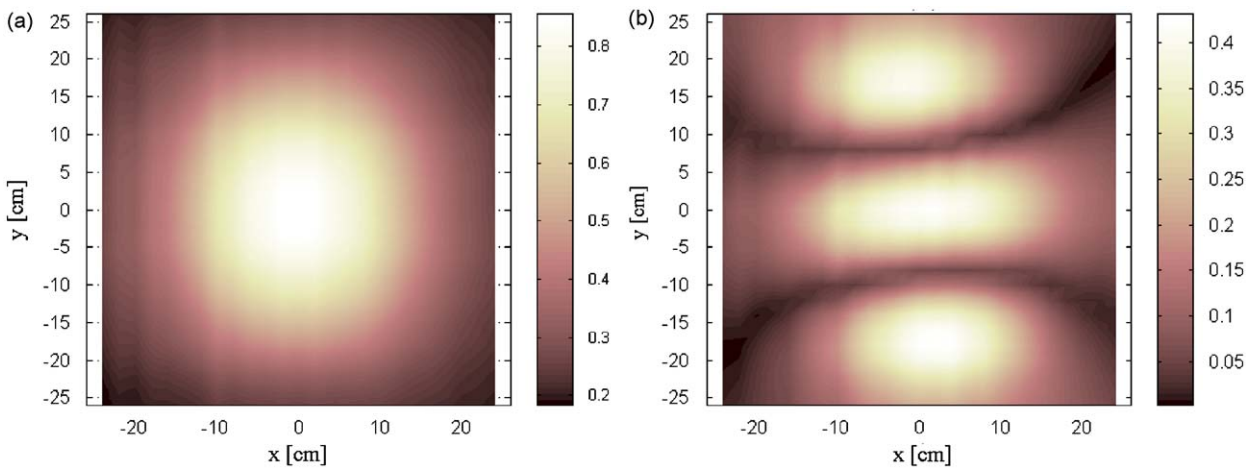

Fig. 4. Baffled plate, measured pressure on hologram plane: (a) $|p|$, 163 Hz and (b) $|p|$, 580 Hz.

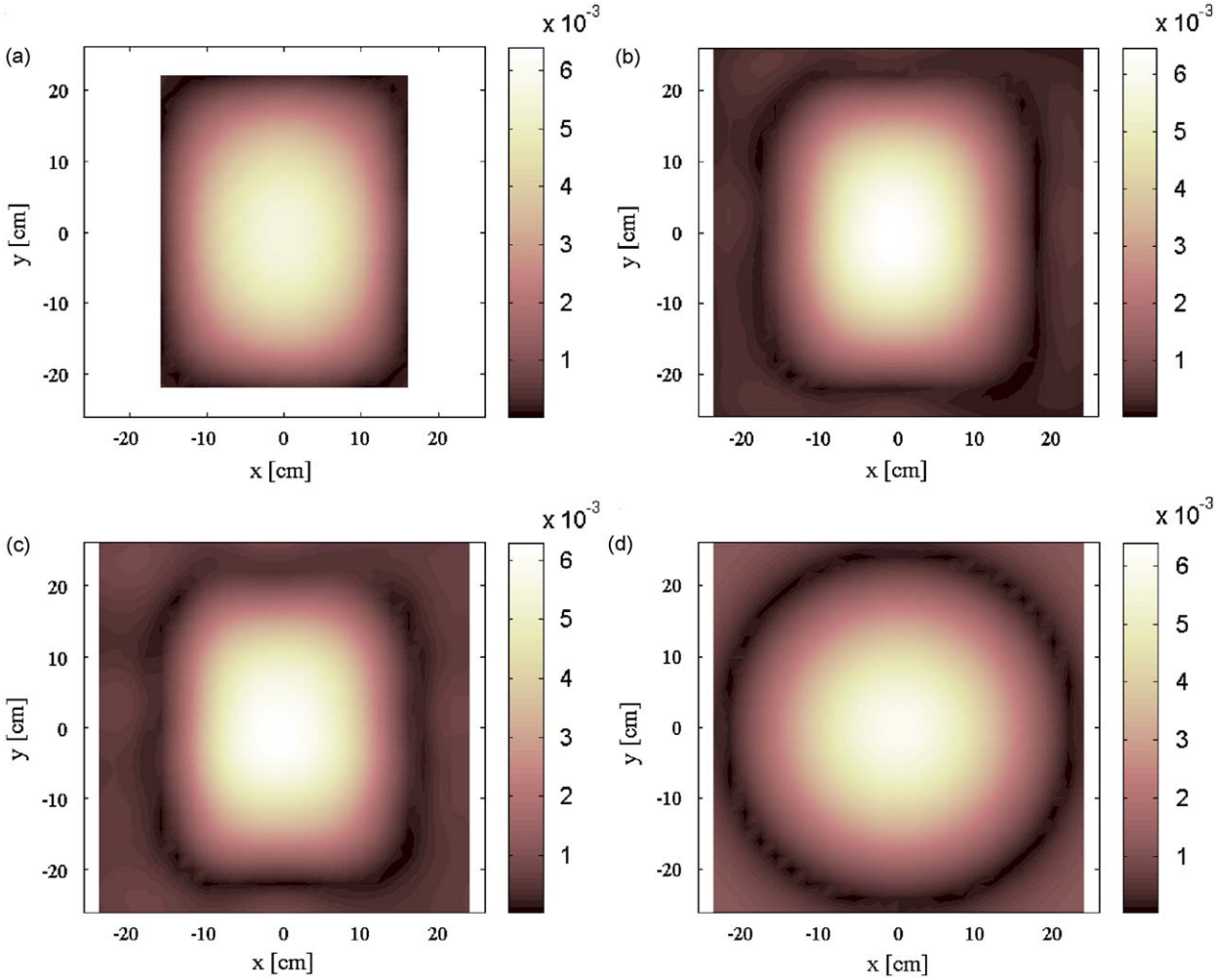

Fig. 5. Baffled plate, measured and reconstructed particle velocity on source plane using inverse Rayleigh, SONAH and conventional NAH at 163 Hz: (a) $|u_z|$, measured; (b) $|u_z|$, inverse Rayleigh; (c) $|u_z|$, SONAH; and (d) $|u_z|$, NAH.

the source region, at both frequencies. In particular, the back-projected velocity calculated using NAH suggests that the source is circular at 163 Hz, while it is actually (based on the directly measured velocity) rectangular.

When compared to the peak pressure level at the center of the plate, the level of the measured pressure at the hologram edge at 163 Hz is lower than that at 580 Hz. But the back-projected particle velocity obtained using NAH is more accurate at 580 Hz than at 163 Hz, which is not typical. The pressure distribution in the y-direction was not affected by spatial truncation as much as that in x-direction. It is possible that the spatial truncation effect of the measurement is less evident when certain higher mode shapes are considered. This is due to a repeated mode shape as illustrated by the 580 Hz case.

4. Baffled plate numerical simulation

A numerical simulation of the baffled plate was performed to confirm the accuracy of the source particle velocity prediction based on near-field measurements both with known signal-to-noise ratios and without any measurement noise. The geometry of the near-field measurements was the same as in the experimental

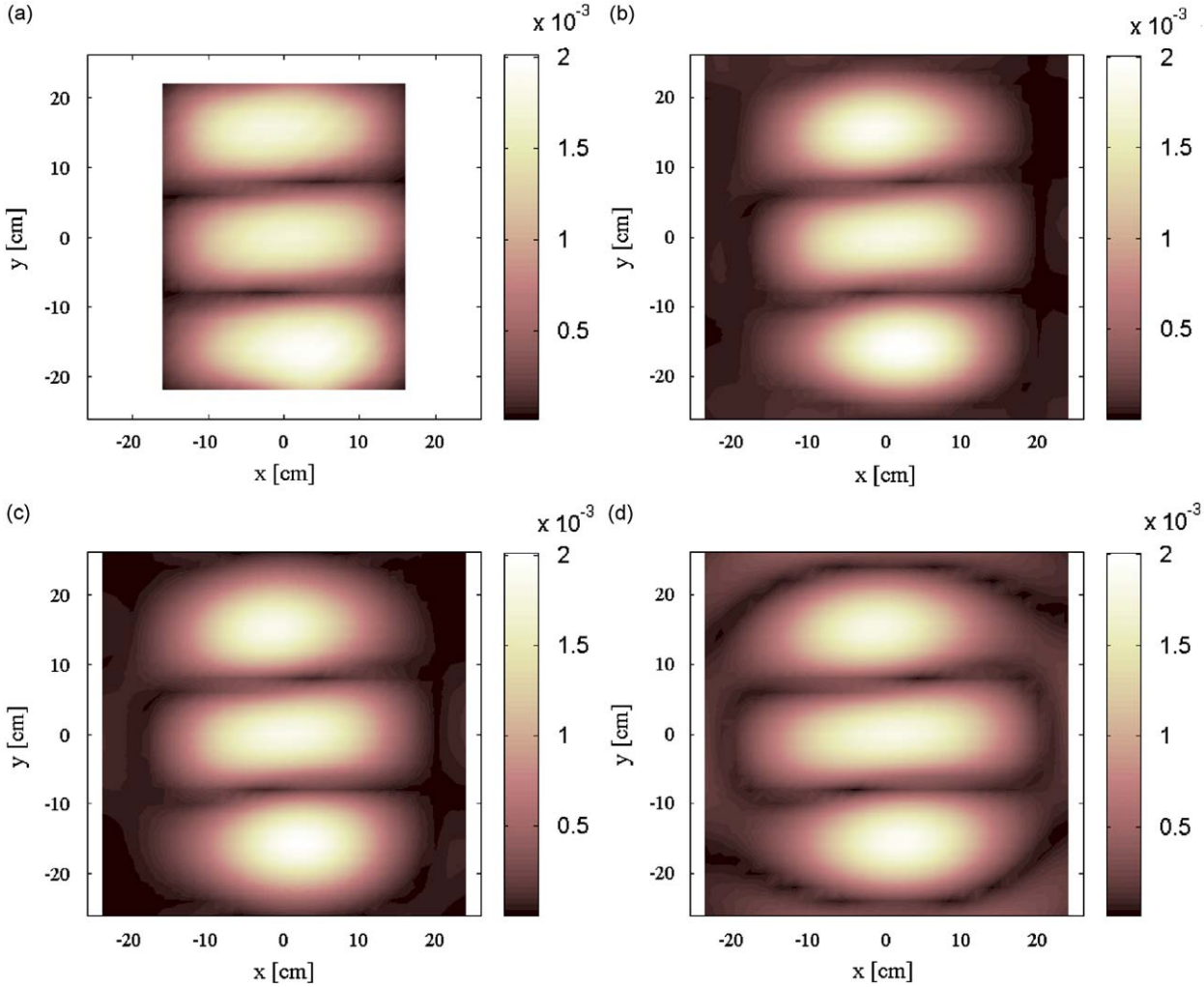

Fig. 6. Baffled plate, measured and reconstructed particle velocity on source plane using inverse Rayleigh, SONAH and conventional NAH at 580 Hz: (a) $|u_z|$, measured; (b) $|u_z|$, inverse Rayleigh; (c) $|u_z|$, SONAH; and (d) $|u_z|$, NAH.

Table 1
Mean square error between source particle velocity prediction based on near-field measurements and actual measurements on baffled plate using the accelerometers and corresponding filtering parameters.

f (Hz)	Inv. Rayl. (%)	SONAH (%)	NAH (%)
163	12.4 ($d = -5$ cm, $\theta = 10$ dB)	11.4 ($d = -10$ cm, $\theta = 10$ dB)	36.6 ($k_c = 15$ rad/m)
580	12.9 ($d = -3$ cm, $\theta = 10$ dB)	13.4 ($d = -10$ cm, $\theta = 10$ dB)	21.7 ($k_c = 28$ rad/m)

baffled plate measurement described in Section 3, except that the spacing between hologram and source plane was 2 cm. In addition to a simulation that reproduced the experimental geometry, a simulation was generated with a hologram surface that was five times larger in both directions than the original hologram surface.

4.1. Baffled plate numerical simulation description

The particle velocity of the baffled plate was simulated by using a combination of sinusoidal functions, given by

$$\begin{aligned}\mathbf{u}_{z,s}(x_s, y_s) &= \sin(m\pi x_s/L_x)\sin(n\pi y_s/L_y) \quad (\text{for } 0 \leqslant x_s \leqslant L_x \text{ and } 0 \leqslant y_s \leqslant L_y)\\ &= 0 \quad (\text{otherwise})\end{aligned} \tag{25}$$

for the (m, n) mode of the plate with dimensions L_x and L_y.

The near-field pressure was calculated by using the simulated source particle velocity combined with the Rayleigh integral given by Eqs. (13) or (17). In order to estimate the discretized Rayleigh integral more accurately for the purpose of generating simulated near-field pressure, evaluation point spacings in the source plane were made smaller than in the hologram plane. First and second order interpolation functions were implemented for integration. Small differences between the pressure generated using first and second order interpolation function were observed when the evaluation point spacing on source plane was 2 cm. As the spacing on the source plane was reduced, the difference between the pressure generated using first and second order interpolation functions became negligible. The final choice of evaluation point spacing on the source plane was 0.2 cm in both the x- and y-directions for the near-field pressure generation. For the simulated particle velocity measurements on the source plane, a measurement spacing of 2 cm was used to compare with prediction, just as in the actual measurements with accelerometers in Section 3.

4.2. Baffled plate numerical simulation results

The mean square error between true and predicted (via simulation) source particle velocities is shown in Tables 2 and 3. Cases with and without random noise added to the measurement pressure were considered in the simulation. The mean square prediction error of the inverse Rayleigh method is slightly smaller than that of SONAH, but the mean square prediction error of NAH is much larger than that of either the inverse Rayleigh method or of SONAH for both cases with and without measurement noise. The mean square prediction error of NAH is almost unchanged by adding 20 dB SNR random noise to the measurement pressure: see Table 3. The latter observation provides evidence that measurement noise up to 20 dB SNR does not contribute significantly to the overall prediction error for the source type and measurement geometry considered in the simulation. Rather, the more dominant source of the projection error when using NAH is due to spatial truncation effects. If the size of original hologram is increased by five times in the x- and y-directions, the NAH error is reduced and becomes similar to those of the inverse Rayleigh and SONAH methods for both cases with and without random noise added to the measurement pressure, as shown in Tables 2 and 3. So the major cause of the NAH projection error is confirmed to be spatial truncation.

Table 2
Mean square error between source particle velocity prediction based on simulated noise free near-field measurements and true velocity.

Mode shape	f (Hz)	Inv. Rayl. (%)	SONAH (%)	NAH (%)	NAH Lg. (%)
(1,1)	163	0.53	1.59	36.7	1.00
(1,3)	580	0.54	0.60	17.7	0.63

Table 3
Mean square error between source particle velocity prediction based on simulated near-field measurements with 20 dB SNR random noise and true velocity.

Mode shape	f (Hz)	Inv. Rayl. (%)	SONAH (%)	NAH (%)	NAH Lg. (%)
(1,1)	163	7.99	9.19	36.9	8.34
(1,3)	580	9.10	9.91	18.1	8.26

Table 4
Mean square error between source particle velocity prediction based on simulated noise free near-field measurements using NAH and true velocity by artificially changing mode shapes.

f (Hz)	163	163	163	580	580	580
Mode shape	(1,1)	(1,3)	(3,3)	(1,1)	(1,3)	(3,3)
MSE (%)	36.7	22.2	14.8	34.1	17.7	12.8

Although not illustrated in the present work, it was found that the mean square back projection error also depends on source and measurement geometry: i.e., the mean square error increases as higher source wave number content is introduced and the measurement surface is placed further away from the source.

As shown in Tables 2 and 3, the mean square error of NAH with the original hologram at 580 Hz is much lower than that at 163 Hz. This difference is not apparent in the results obtained using the inverse Rayleigh and SONAH procedures, and NAH with a larger hologram. To confirm whether the mean square error of NAH is related more to frequency than to mode shapes, a numerical simulation was performed with an artificial combination of two frequencies and three different mode shapes. The mean square error of NAH with three different mode shapes, (1,1), (1,3) and (3,3), at frequencies of 163 and 580 Hz is shown in Table 4. It can be seen that the mean square error of NAH is much more sensitive to mode shape than frequency, an effect that is possibly related to the performance of the Tukey window. True and reconstructed particle velocities on the source plane obtained by using the inverse Rayleigh and SONAH procedures, and conventional NAH with original and larger holograms at 163 and 580 Hz are shown in Figs. 7 and 8, respectively. Some details of the source are lost during the reconstruction due to the 20 dB SNR random noise added to the measurement pressure: that is true for all reconstruction procedures. However, more details about the source were obtained by using the inverse Rayleigh and SONAH procedures than when using conventional NAH, especially at 163 Hz in the vicinity of the source edge when the pressure was measured with the original hologram size. As shown in Fig. 7(d), the mode shape of source particle velocity reconstructed using conventional NAH with the original hologram size is very close to circular instead of rectangular, especially at the edge of the source. However, the shape of the source particle velocity reconstructed using conventional NAH with a larger hologram size is very similar to true source particle velocity.

5. Multi-pole numerical simulation

A multi-pole numerical simulation was performed to confirm the accuracy of source particle velocity prediction based on near-field measurements both with known signal-to-noise ratios and without any measurement noise. The major difference with the baffled plate simulation in Section 4 is that the multi-pole numerical simulation was performed without any baffle, in which case the Rayleigh integral is not valid. The accuracy of the various procedures was compared over a range of frequencies. The geometry of near-field measurements was the same as the baffled plate numerical simulation described in Section 4. The simulation was used to compare the relative accuracies of inverse Rayleigh, SONAH, and NAH in predicting source particle velocity by using the original and the larger hologram surfaces.

5.1. Multi-pole numerical simulation description

The radiated pressure was generated by using a multi-pole that consisted of ten randomly located in- or out-of-phase coherent monopoles each with unit amplitude. The locations and phases of the 10 monopoles used in the multi-pole simulation are shown in Table 5. All of the monopoles were located at either $z = -5$ or -7 cm, and within a 17 cm $\times$ 23 cm rectangle centered at the z-coordinate axis. The multi-pole was made to fit inside an area that was 25 percent of the original hologram surface area in order to reduce truncation effects at the edges of the hologram.

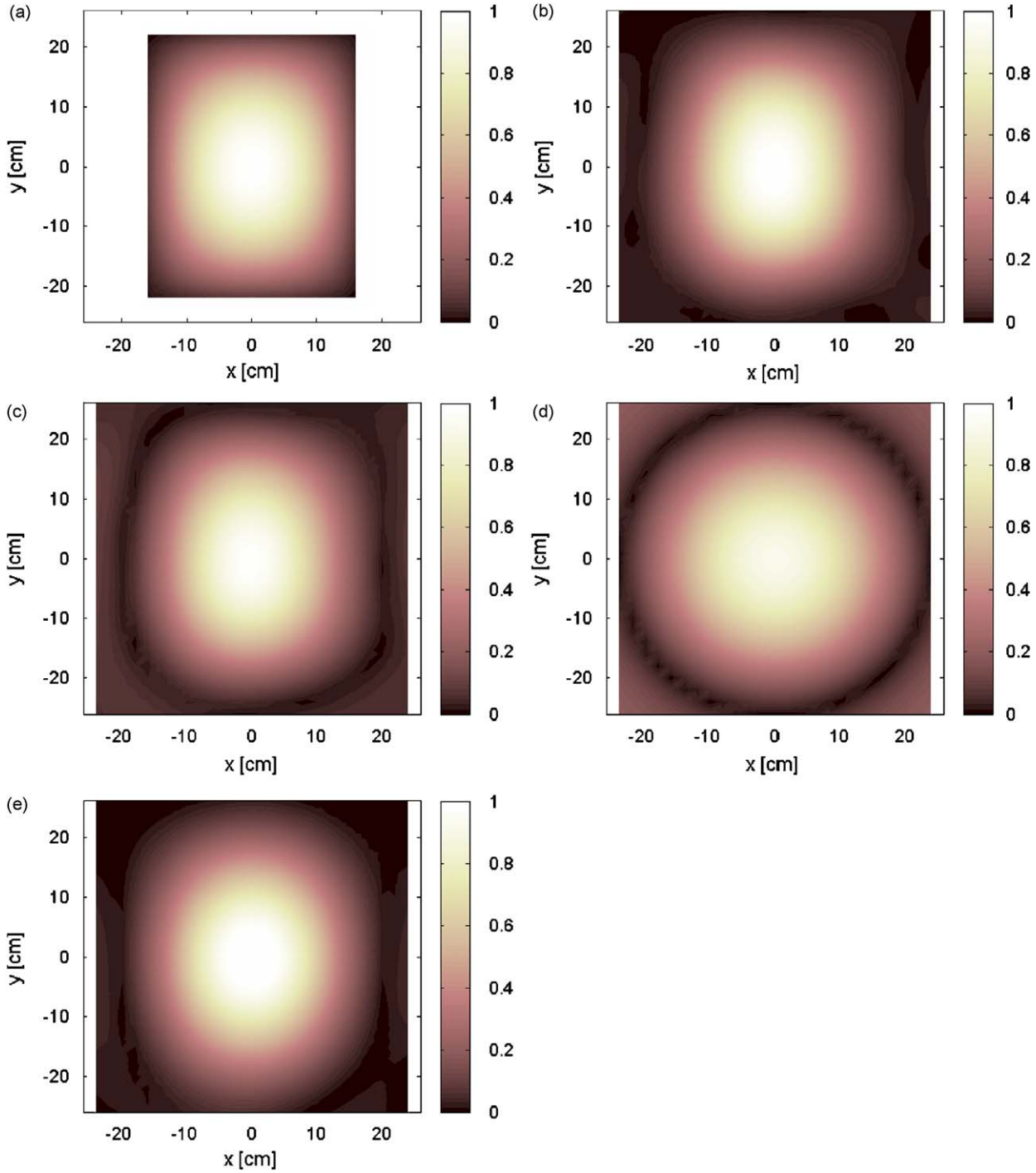

Fig. 7. Simulated baffled plate, true and reconstructed particle velocity on source plane using inverse Rayleigh, SONAH and conventional NAH at 163 Hz measured with 20 dB SNR random noise: (a) $|u_z|$, true; (b) $|u_z|$, inverse Rayleigh; (c) $|u_z|$, SONAH; (d) $|u_z|$, NAH; and (e) $|u_z|$, NAH with larger measurement aperture.

The particle velocities at the $z = 0$ plane were generated by using Euler's equation on a plane the same size as the baffled plate simulation shown in Section 4. The near-field pressures were generated with and without 20 dB SNR random noise with identical hologram size and location as in the baffled plate simulation shown in

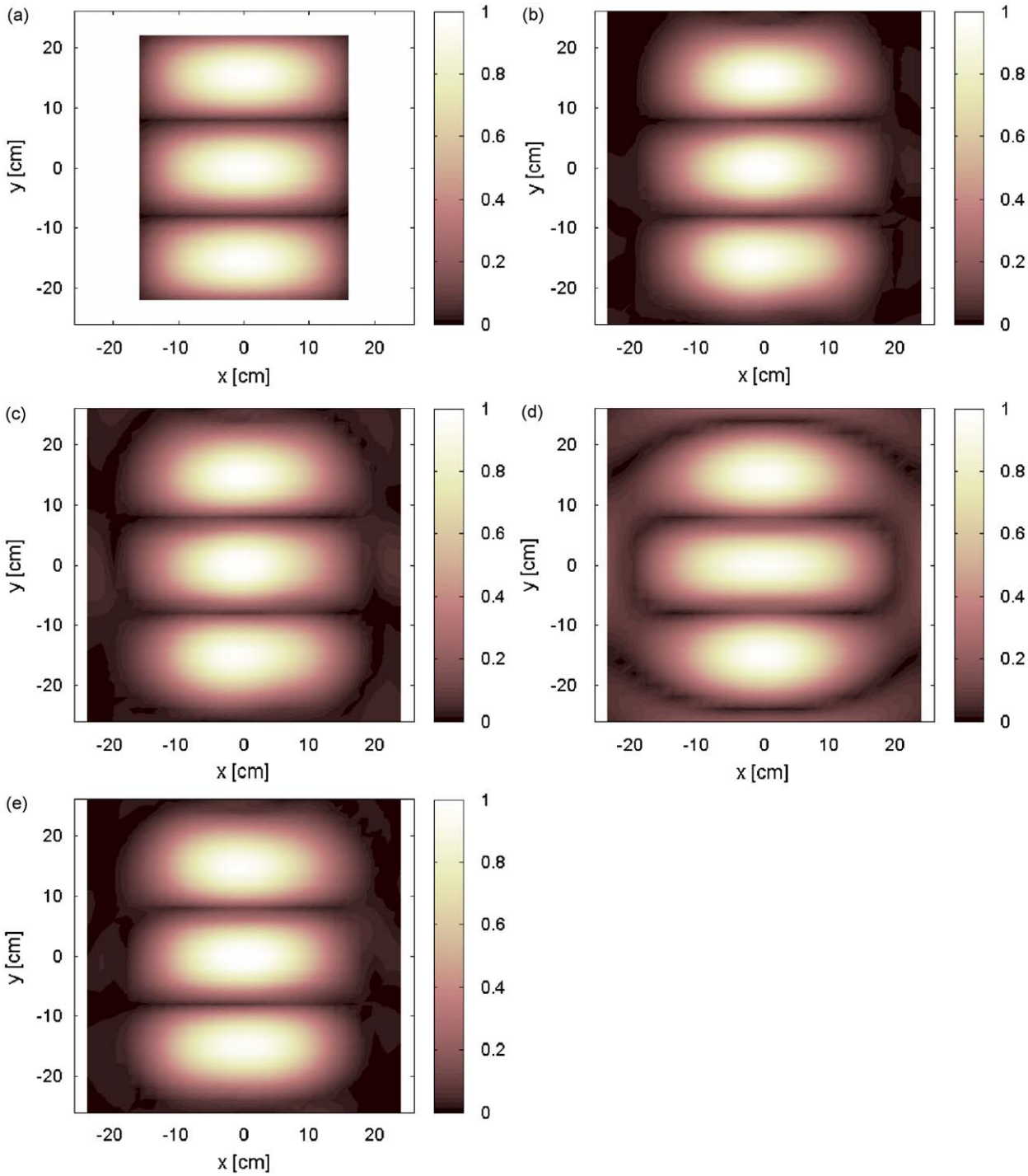

Fig. 8. Simulated baffled plate, true and reconstructed particle velocity on source plane using inverse Rayleigh, SONAH and conventional NAH at 580 Hz measured with 20 dB SNR random noise: (a) $|u_z|$, true; (b) $|u_z|$, inverse Rayleigh; (c) $|u_z|$, SONAH; (d) $|u_z|$, NAH; and (e) $|u_z|$, NAH with larger measurement aperture.

Section 4. The particle velocity was predicted at the $z = 0$ plane from near-field measurement by using NAH, SONAH and the inverse Rayleigh method. The mean square percentage error between the predicted and true velocities was evaluated with and without measurement noise.

Table 5
Location and strength of ten coherent monopoles used in multi-pole simulation.

(x,y,z) (cm)	Q
(−7.0,8.2,−5)	1
(−0.7,7,−7)	1
(−2.1,3.2,−7)	−1
(−6.4,−4.2,−7)	−1
(−2.2,−8.2,−5)	1
(1,−4.2,−5)	−1
(2.2,−1.9,−7)	1
(5.9,−8.1,−5)	−1
(2.8,3.4,−5)	1
(6.1,9.8,−7)	−1

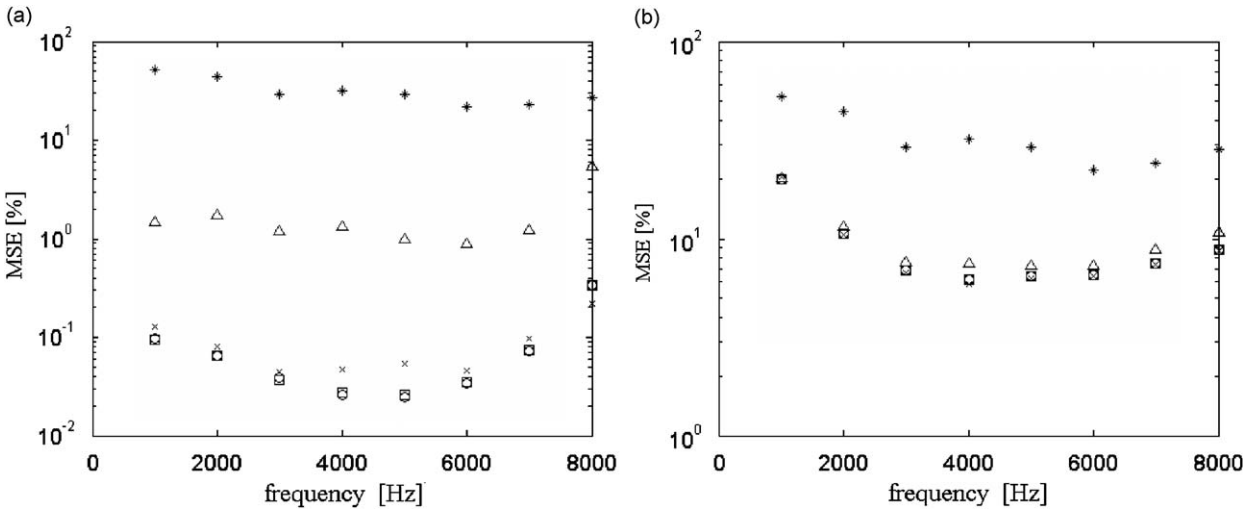

Fig. 9. Multi-pole simulation, mean square error between true particle velocity and prediction from near-field pressure measurement in terms of frequencies using inverse Rayleigh with first and second order interpolation functions, conventional NAH with identical and larger measurement aperture, and SONAH procedures. o inverse Rayleigh (first order estimation): □: inverse Rayleigh (second order estimation); *: NAH; ×: NAH (larger hologram); Δ: SONAH. (a) Percentage mean square error, measurement without noise and (b) percentage mean square error, measurement with 20 dB random noise.

5.2. Multi-pole numerical simulation results

The multi-pole numerical simulation was performed at eight frequencies from 1000 to 8000 Hz, where the Nyquist cutoff frequency for spatial sampling was 8575 Hz. The multi-pole measurement pressure in the x- and y-directions was observed to be highly frequency dependent. The mean square error between the directly measured and predicted particle velocities estimated from the near-field pressure measurements is shown in Fig. 9. The percentage mean square error was calculated at eight frequencies with and without 20 dB SNR random measurement noise. The mean square prediction error obtained when using either NAH with the larger hologram or the inverse Rayleigh method (with first and second order interpolation functions for evaluating the integrals) was almost identical over the range of frequencies considered. The mean square prediction error of NAH with the original sized hologram was the largest regardless of frequency and SNR level. The performance of SONAH, shown in Fig. 9(a), in terms of mean square prediction error, is much better than that of NAH. With the exception of the 8000 Hz case, the SONAH mean square error was between one and two percent. The prediction error obtained by using all of procedures except NAH is very similar for

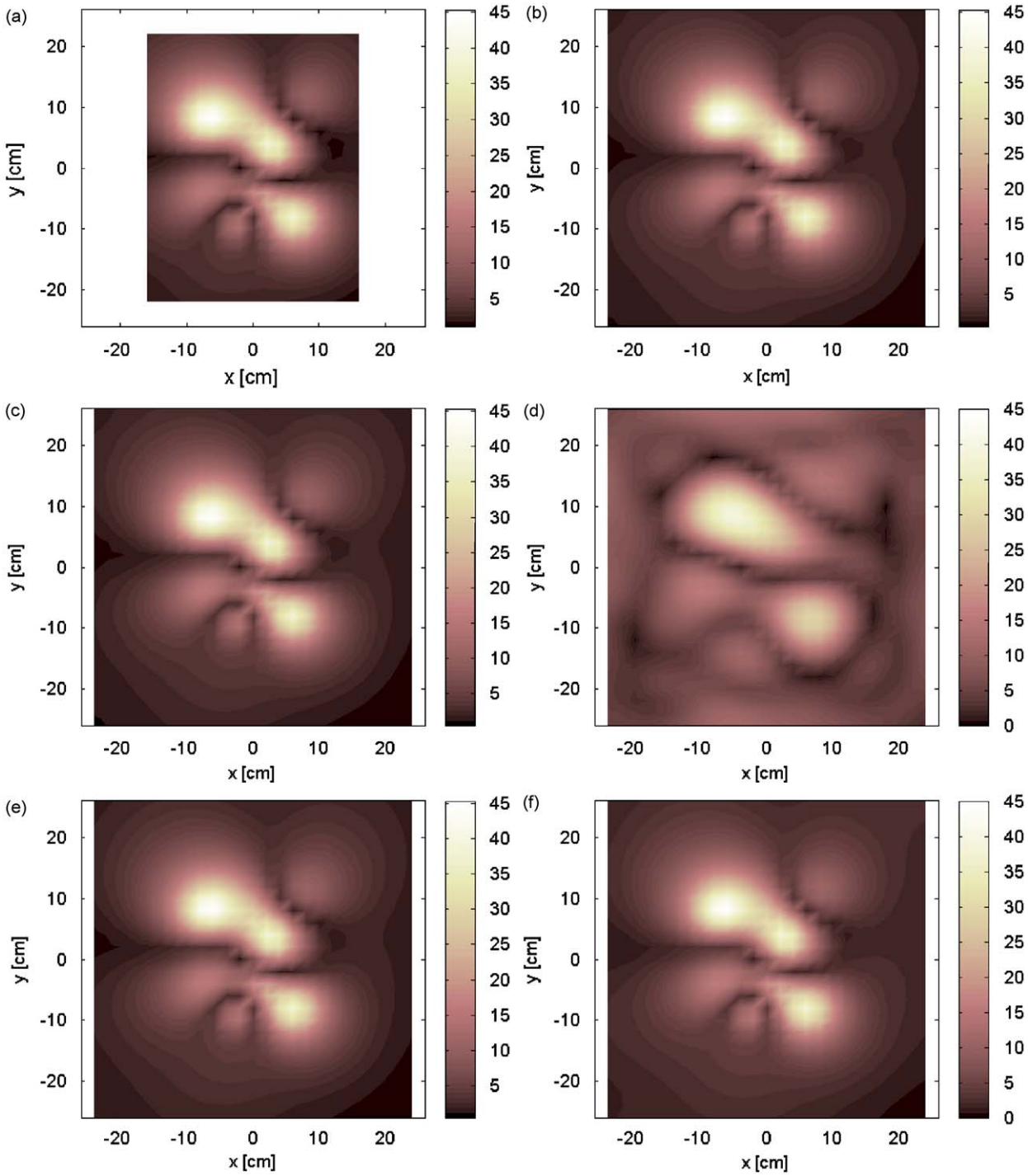

Fig. 10. Multi-pole simulation, true particle velocity and prediction from near-field pressure measurement at 1000 Hz without measurement noise: (a) true; (b) inverse Rayleigh, first order; (c) inverse Rayleigh, second order; (d) conventional NAH; (e) NAH with expanded measurement aperture; and (f) SONAH.

most of the frequencies both with and without measurement noise. Since the prediction error obtained using NAH with the larger hologram is as accurate as those of inverse Rayleigh, and SONAH procedures, it can be concluded that the spatial limitation of the original sized NAH hologram was the major cause of error.

True and predicted particle velocities at 1000 Hz obtained by using the NAH, SONAH, and inverse Rayleigh procedures without measurement noise is shown in Fig. 10. The errors of all prediction procedures excluding NAH with the original hologram size are practically identical except around the edge of the hologram. This is confirmed by the mean square errors shown in Fig. 9.

6. Conclusions

The normal particle velocity on or closer to the source plane can be predicted based on near-field pressure measurements by using NAH, SONAH, and the inverse Rayleigh procedures. It was found that the prediction error of NAH was the largest amongst the procedures considered in this work when all the measurements were made on the same hologram surface. The particle velocity prediction error obtained when using NAH with a larger hologram surface, SONAH, and the inverse Rayleigh method were very similar overall.

The inverse Rayleigh results can be estimated very efficiently by avoiding repeated calculations when estimating the transfer matrix between the fictitious source velocity on the virtual source plane and the measured or reconstructed pressure. The accuracy of the inverse Rayleigh method is comparable to that of SONAH, and NAH with a larger hologram surface. This has been shown for numerical simulation cases with and without measurement noise in addition to actual baffled plate measurements. The inverse Rayleigh method was also used to predict the particle velocity from multi-pole near-field pressure measurements without any baffle and was found to be accurate over a range of frequencies. It can be concluded that the inverse Rayleigh method is valid for general cases of sources with or without an infinite baffle.

The source velocities estimated using SONAH and the inverse Rayleigh method based on near-field experimental measurements were reasonably accurate even though there was some discrepancy in the peak level of the baffled plate velocity. This result may be partly due to the use of different types of transducers calibrated at two different frequencies for velocity and pressure measurements. The accuracy of SONAH and the inverse Rayleigh method for source particle velocity prediction were very similar according to the results of numerical simulations and measurement in an anechoic chamber. Thus the main conclusion of the present work is that both SONAH and the inverse Rayleigh method provide a useful set of tools that are as accurate as NAH (when performed with a much larger measurement aperture) for source identification and prediction of the sound field.

Appendix A

In this section, the partial derivative of the fictitious source particle velocity is presented to allow the estimation of the relative accuracy of the relation between source property and measurement pressure by assuming a fictitious source particle velocity as the source property independent of measurement location. The partial derivative of the fictitious source particle velocity shown in Eq. (11) with respect to z, is expressed as

$$\frac{\partial}{\partial z}\mathbf{u}_{\mathrm{fic},z}(\mathbf{r}_{s,v},\mathbf{r}) = \frac{\partial}{\partial z}\left[\frac{p(\mathbf{r}_{s,v})}{\rho c}\left(\frac{1}{\mathrm{i}kR_v}-1\right)\frac{z_{s,v}-z}{R_v}+u_z(\mathbf{r}_{s,v})\right], \tag{A.1}$$

which reduces to,

$$\frac{\partial}{\partial z}\mathbf{u}_{\mathrm{fic},z}(\mathbf{r}_{s,v},\mathbf{r}) = \frac{p(\mathbf{r}_{s,v})}{\rho c}\left[\left(\frac{1}{\mathrm{i}kR_v}+1\right)\frac{1}{R_v}+\left(\frac{2}{\mathrm{i}kR_v}-1\right)\frac{(z_{s,v}-z)^2}{R_v^3}\right]. \tag{A.2}$$

The definition of the source and near-field measurement geometry with the virtual source plane for estimation of the derivative of the fictitious source particle velocity is shown in Fig. A1. The normalized amplitude of the derivative of the fictitious source particle velocity in terms of the virtual source plane location, $z_{s,v}$, angle, θ, in the normal direction to the measurement plane, frequency, and measurement surface location z is shown in Fig. A2. The amplitude of the derivative is normalized for $z_{s,v} = -0.02$ m, $\theta = 45°$, frequency = 1000 Hz, and $z = 0.1$ m. The amplitude of the derivative of the fictitious source particle velocity is a maximum when $z_{s,v} = 0$, i.e., when the virtual source plane is located at the actual source location, and reduces as the virtual source plane is moved away from the actual source location. The amplitude of the derivative of fictitious source particle velocity is a maximum at $\theta = 0$, $z = 0.05$ m, and at the lowest frequency, and is relatively constant except at low frequencies.

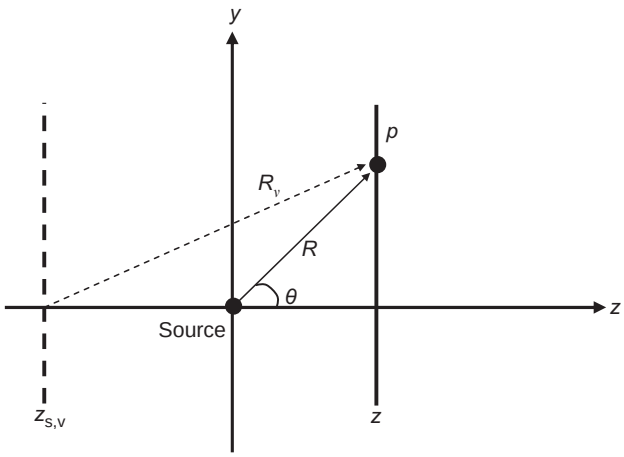

Fig. A1. Definition of source and near-field measurement geometry with virtual source plane for estimation of derivative of fictitious source particle velocity.

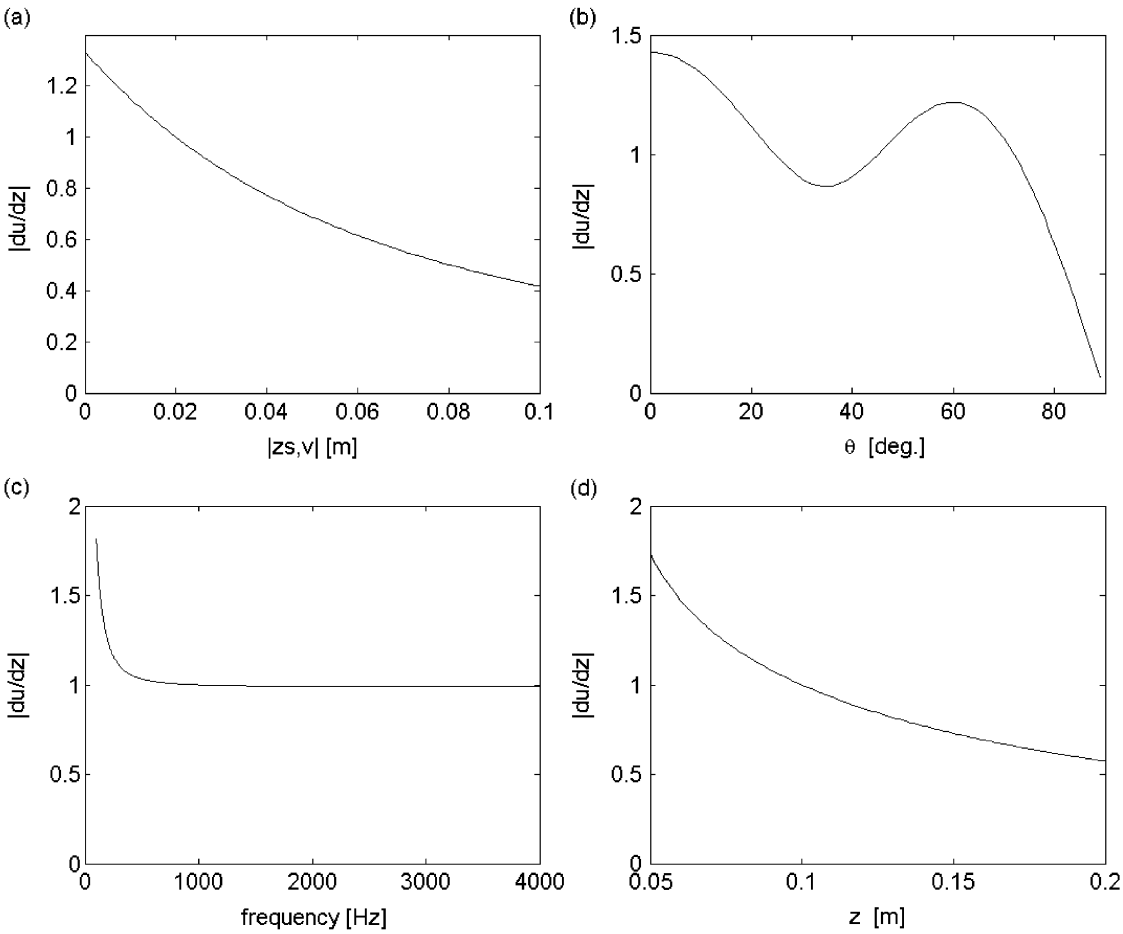

Fig. A2. Normalized amplitude of derivative of fictitious source particle velocity in terms of different variables: (a) $|z_{s,v}|$; (b) θ; (c) frequency; and (d) z.

References

[1] J.D. Maynard, E.G. Williams, Y. Lee, Nearfield acoustic holography: I. Theory of generalized holography and the development of NAH, *Journal of the Acoustical Society of America* 78 (1985) 1395–1414.

[2] E.G. Williams, H.D. Dardy, K.B. Washburn, Generalized near-field acoustic holography for cylindrical geometry: theory and experiment, *Journal of the Acoustical Society of America* 81 (1987) 389–407.

[3] E.G. Williams, *Fourier Acoustics: Sound Radiation and Near-field Acoustical Holography*, Academic Press, New York, 1999.

[4] R. Steiner, J. Hald, Near-field acoustical holography without the errors and limitations caused by the use of spatial DFT. *Proceedings of ICSV6*, 1999, pp. 843–850.

[5] J. Hald, Patch near-field acoustical holography using a new statistically optimal method, *Proceedings of Inter-Noise 2003*, Seogwipo, Korea, 2003, pp. 2203–2210.

[6] Y.T. Cho, J.S. Bolton, J. Hald, Source visualization by using statistically optimized near-field acoustical holography in cylindrical coordinates, *Journal of the Acoustical Society of America* 118 (2005) 2355–2365.

[7] K. Saiyou, S. Yoshikawa, Reduction methods of the reconstruction error for large-scale implementation of near-field acoustical holography, *Journal of the Acoustical Society of America* 110 (2001) 2007–2023.

[8] K. Saiyou, H. Uchida, Data extrapolation method for boundary element method-based near-field acoustical holography, *Journal of the Acoustical Society of America* 115 (2004) 785–796.

[9] E.G. Williams, B.H. Houston, P.C. Herdic, Fast Fourier transform and singular value decomposition formulations for patch nearfield acoustical holography, *Journal of the Acoustical Society of America* 114 (2003) 1322–1333.

[10] M. Lee, J.S. Bolton, Patch near-field acoustical holography in cylindrical geometry, *Journal of the Acoustical Society of America* 118 (2005) 3721–3732.

[11] M. Lee, J.S. Bolton, Reconstruction of source distributions from sound pressures measured over discontinuous regions: multipatch holography and interpolation, *Journal of the Acoustical Society of America* 121 (2007) 2086–2096.

[12] A. Sarkissian, Extension of measurement surface in near-field acoustic holography, *Journal of the Acoustical Society of America* 115 (2004) 1593–1596.

[13] A. Sarkissian, Method of superposition applied to patch near-field acoustic holography, *Journal of the Acoustical Society of America* 118 (2005) 671–678.

[14] Z. Wang, S.F. Wu, Helmholtz equation—least-squares method for reconstructing the acoustic pressure field, *Journal of the Acoustical Society of America* 102 (1997) 2020–2032.

[15] S.F. Wu, X. Zhao, Combined Helmholtz equation—least-squares method for reconstructing acoustic radiation from arbitrarily shaped objects, *Journal of the Acoustical Society of America* 112 (1997) 179–188.

[16] T. Semenova, S.F. Wu, The Helmholtz equation—least-squares method and Rayleigh hypothesis in near-field acoustical holography, *Journal of the Acoustical Society of America* 115 (2004) 1632–1640.

[17] T. Semenova, S.F. Wu, On the choice of expansion functions in the Helmholtz equation least-squares method, *Journal of the Acoustical Society of America* 117 (2005) 701–710.

[18] Y.T. Cho, Holographic Projection of Sound Fields Based on Spatially-limited Data Sets, PhD Dissertation, Purdue University, West Lafayette, IN, 2006.

[19] M. Lee, J.S. Bolton, A one-step patch near-field acoustical holography procedure, *Journal of the Acoustical Society of America* 122 (2007) 1662–1670.

[20] E.G. Williams, J.D. Maynard, Numerical evaluation of the Rayleigh integral for planar radiators using the FFT, *Journal of the Acoustical Society of America* 72 (1982) 2020–2030.

[21] J.W. Wind, Y.H. Wijnant, A. de Boer, Fast evaluation of the Rayleigh integral and applications to inverse acoustics, *Proceedings of ICSV13*, Vienna, Austria, 2006.

[22] G.H. Koopmann, L. Song, J.B. Fahnline, A method for computing acoustic fields based on the principle of wave superposition, *Journal of the Acoustical Society of America* 86 (1989) 2433–2438.

[23] A.D. Pierce, *Acoustics: An Introduction to its Physical Principle and Applications*, Acoustical Society of America, New York, 1991.

[24] P.M. Morse, K.U. Ingard, *Theoretical Acoustics*, Princeton University Press, Princeton, 1968.

[25] H. Holste, An equivalent source method for calculation of the sound radiated from aircraft engines, *Journal of Sound and Vibration* 203 (1997) 667–696.

[26] M.E. Johnson, S.J. Eliott, K.-H. Baek, J. Garcia-Bonito, An equivalent source technique for calculating the sound field inside an enclosure containing scattering objects, *Journal of the Acoustical Society of America* 104 (1998) 1221–1231.

[27] N.P. Valdivia, E.G. Williams, Study of the comparison of the methods of equivalent sources and boundary element methods for near-field acoustic holography, *Journal of the Acoustical Society of America* 120 (2006) 3694–3705.

[28] P.A. Nelson, S.H. Yoon, Estimation of acoustic source strength by inverse methods: part I, conditioning of the inverse problem, *Journal of Sound and Vibration* 233 (2000) 643–668.

[29] Y.T. Cho, J.S. Bolton, M.J. Roan, Far-field pressure prediction based on near-field measurements using acoustical holography, *Journal of Sound and Vibration*, to be submitted.

[30] L.J. Sergerlind, *Applied Finite Element Analysis*, Wiley & Sons, Inc., New York, 1984.

[31] B.T. Phong, Illumination for computer generated pictures, *Communications of the ACM* 18 (1975) 311–317.